

## ORIGINAL ARTICLE

# Dual-band polarization-insensitive orbital angular momentum beam generation based on 1-bit polarization-converting transmitting coding metasurface

Junfeng Li<sup>1</sup> | Xianglin Kong<sup>1</sup> | Jun Wang<sup>1</sup> | Zhuwei Miao<sup>2</sup> |  
Xiaoyi Wang<sup>3</sup> | Xiaopeng Shen<sup>4</sup>  | Lei Zhao<sup>1</sup>

<sup>1</sup>School of Information and Control Engineering, China University of Mining and Technology, Xuzhou, China

<sup>2</sup>State Key Laboratory of Millimeter Waves, School of Information Science and Engineering, Southeast University, Nanjing, China

<sup>3</sup>Department of Electrical Engineering, Polytechnique Montreal, Montreal, Quebec, Canada

<sup>4</sup>School of Materials Science and Physics, China University of Mining and Technology, Xuzhou, China

## Correspondence

Lei Zhao, School of Information and Control Engineering, China University of Mining and Technology, Xuzhou 221116, China.

Email: leizhao@cumt.edu.cn

## Funding information

National Natural Science Foundation of China, Grant/Award Number: 61771226

## Abstract

This article presents a polarization-insensitive 1-bit coding metasurface (CM) for dual-band orbital angular momentum (OAM) beam generation. The metasurface unit cell is composed of two symmetric metal layers, which are separated by a dielectric substrate. Each metal layer consists of an outer square ring, a middle square ring, and an inner rhombus patch. By rotating the direction of the inner rhombus patch to 0° and 90°, two states with out-of-phase transmitting responses for both bands are achieved. An equivalent circuit is proposed to analyze the design. The OAM beams are then realized by properly distributing the two states on the metasurface aperture. A metasurface with 30 × 30 elements is designed, simulated, and experimentally demonstrated. The experimental results agree well with the simulating ones, showing that 3-dB transmission bandwidths of 13.6–14.8 GHz and 26.7–27.7 GHz are realized in both Ku and Ka bands, with the mode purities 0.89 and 0.73, respectively.

## KEYWORDS

coding metasurface (CM), dual-band, mode purities, orbital angular momentum (OAM), polarization-insensitive

## 1 | INTRODUCTION

Orbital angular momentum (OAM) is a type of electromagnetic wave that uses light waves to produce a unique spiral wavefront, identified by Allen et al.<sup>1</sup> OAM wavefront presents the features of spiral phase distribution and a phase singularity, which can be described by the azimuth phase term  $\exp(-jl\varphi)$  (where  $l$  is the mode number of OAM and  $\varphi$  the azimuth).<sup>2</sup> Due to the unique orthogonal property of different eigenstates of OAM beams, OAM has become a hot research topic gradually and has been widely applied in various fields of quantum information, holographic imaging, astrophysics, applied optics, and wireless multiplexing.<sup>3–9</sup>

There are numerous ways to obtain OAM beams in the radio frequency, such as spiral phase plates,<sup>10</sup> and antenna arrays.<sup>11,12</sup> However, there are several different issues in the realization of OAM beams. For instance, the spiral phase plates can only produce narrow-band OAM waves with a single mode, and the antenna arrays require complicated feeding networks, which greatly increase design complexity. Metasurfaces, the two-dimensional counterpart of the bulky metamaterials, have recently been studied to control electromagnetic waves, thanks to their natural features of low cost, low profile, and the strong capability to manipulate electromagnetic waves at smaller and more precise scales.<sup>13–15</sup> Metasurfaces have also been studied for generating OAM beams. For instance, a reflective two-layer OAM

metasurface is proposed using Pancharatnam-Berry (PB) phase, which can be applied to both linearly polarized (LP) and circularly polarized (CP) waves.<sup>16</sup> More PB phase-based reflection-type,<sup>17,18</sup> transmission-type<sup>19–23</sup> and multi-band devices have been proposed and widely studied,<sup>24–28</sup> thanks to the simplicity of PB phase design and its advantages in the design of ultra-wideband metasurfaces. However, reflective metasurfaces will cause feed blockage, where the reflected wave may be affected by the feeding antenna. In contrast, the incident and transmitted waves are separated in different physical spaces and do not interfere with each other for transmitting metasurfaces.

In recent years, the concept of coding metasurfaces (CM) was proposed to simplify the design of metasurfaces by mapping each unit cell response to an  $N$ -bit state, which provides greater freedom of operation than the traditional metasurfaces.<sup>29</sup> CM has been extensively researched to achieve various electromagnetic characteristics and design different functional devices in the microwave, terahertz, and acoustic regimes.<sup>30–34</sup> Although CMs have already greatly reduced the design complexity of metasurface particles, high-bit CMs still meet many difficulties to achieve complicated amplitude and phase responses. Therefore, 1-bit CMs, the simplest CMs with only two response states, have been attracting more and more attention to realize various functions.<sup>35–37</sup>

In this article, we propose a 1-bit polarization-insensitive transmitting CM using a two-layer structure for dual-band OAM-beam generation. The metasurface is characterized by a low profile, which operates at both the Ku (13.6–14.8 GHz) band and Ka (26.7–27.7 GHz) band with a transmitting efficiency higher than 0.7. The realized mode purities of the two bands are analyzed, respectively, which are 0.89 at Ku-band and 0.73 at Ka-band. Two +1 order OAM beams at the two bands are generated simultaneously. The polarization-insensitive feature is realized due to the cross-polarization transformation during the generation of OAM beams. Two out-of-phase transmitting responses are used in the CM by rotating the inner rhombus patch to  $0^\circ$  and  $90^\circ$ , respectively. An equivalent circuit model is also proposed to analyze the unit cell design. The proposed dual-band OAM metasurface is verified by both full-wave simulation and experimental demonstration in this letter.

## 2 | METASURFACE UNIT CELL DESIGN

### 2.1 | Unit cell design

Figure 1 shows the conceptual illustration of the proposed 1-bit OAM CM with a detailed unit cell structure.

The metasurface unit cell consists of two metal layers, which are separated by a single-layer dielectric substrate (Rogers RO3003,  $\epsilon_r = 3$ , tangent losses = 0.001,  $h = 1.524$  mm). Each of the metal layers is composed of an outer square ring, a middle square ring, and an inner rhombus patch. The symmetric dual-layer design is to introduce two currents flowing in the same direction to enhance the transmitting coefficient.<sup>38</sup> The design parameters of the unit cells are  $p = 10$  mm,  $s = 0.5$  mm,  $b = 8$  mm,  $g = 0.5$  mm,  $l = 8$  mm,  $w = 3$  mm,  $e = 0.5$  mm.

By rotating the inner rhombus patch with an angle of  $90^\circ$ , two out-of-phase transmitting responses are obtained, which are defined as states 0 and 1, respectively. The operating principle of the proposed metasurface may be understood with the help of Figure 2. The electrical field of the  $y$ -polarized incident wave  $\mathbf{E}^i$  is divided into two orthogonal components  $\mathbf{E}_v^i$  and  $\mathbf{E}_u^i$  respectively. For state 0, the incident EM wave can be expressed as

$$\mathbf{E}^i = \mathbf{E}_u^i + \mathbf{E}_v^i = \mathbf{u}E_u^i e^{j\phi} + \mathbf{v}E_v^i e^{j\phi} \quad (1)$$

and the transmitted wave is expressed as

$$\mathbf{E}^t = \mathbf{u}t_u E_u^i e^{j(\phi+\phi_u)} + \mathbf{v}t_v E_v^i e^{j(\phi+\phi_v)} \quad (2)$$

where  $\phi_u$ ,  $\phi_v$  are the phases of the metasurface transmitting coefficients and  $t_u$ ,  $t_v$  are the amplitudes of the metasurface transmitting coefficients along the  $u$ - and  $v$ - axes, respectively.

If the metasurface unit cell is resonant at the  $v$  direction and nonresonant at the  $u$  direction, the transmitting amplitudes  $t_u$ ,  $t_v$  are same, but the transmitting phases  $\phi_u$ ,  $\phi_v$  have a  $180^\circ$  difference.<sup>39</sup> The transmitting electrical field  $\mathbf{E}^t$  composed of  $\mathbf{E}_v^t$  and  $\mathbf{E}_u^t$  is then rotated by  $90^\circ$  clockwise compared to the incident wave  $\mathbf{E}^i$ , suggesting that the unit cell achieves the polarization conversion at the resonant band. To further understand the principle of the polarization conversion, we perform full-wave simulation of the transmitted amplitude and phase responses of the state 0 unit cell under an incident polarization along the  $u$ - and  $v$ - axes, respectively. The full-wave simulation is performed using periodic boundary conditions with the help of the commercial EM simulation software CST Microwave Studio. The simulating results are plotted in Figure 3, showing that the phase difference ( $\Delta\varphi$ ) between  $t_u$  and  $t_v$  by the anisotropy of the metasurface is equal to  $180^\circ$  at the dual-band as expected. Similarly, for state 1, the metasurface also converts the incident wave into cross-polarization at the frequency when the unit cell is resonant at  $u$  direction.<sup>37</sup> The cross-polarization transmitting coefficient for the  $x$ -polarized

FIGURE 1 Conceptual illustration of the proposed 1-bit orbital angular momentum coding metasurface with a detailed unit cell structure

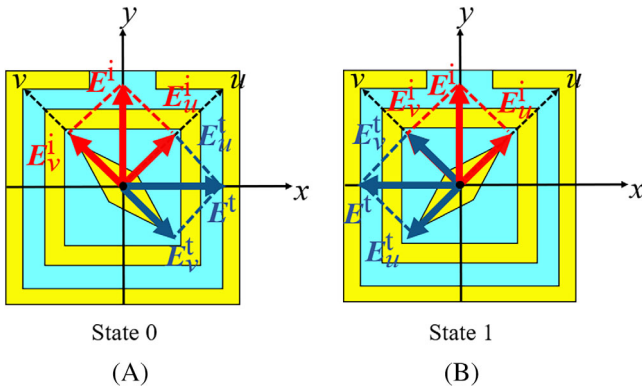
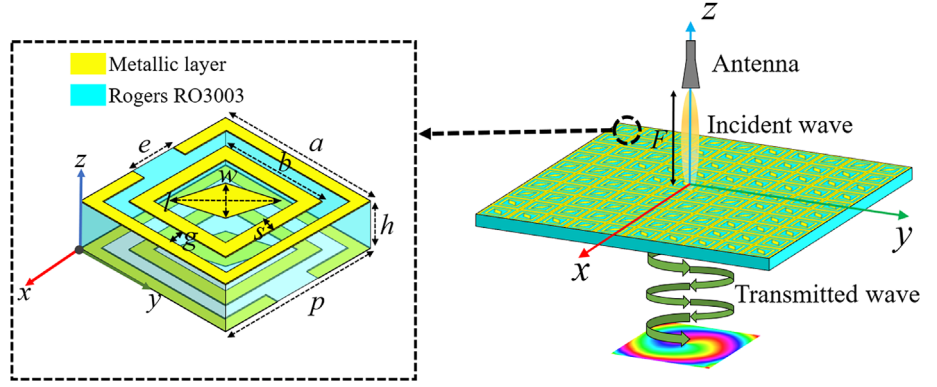


FIGURE 2 Polarization conversion principle of the metasurface unit cell. (A) State 0. (B) State 1

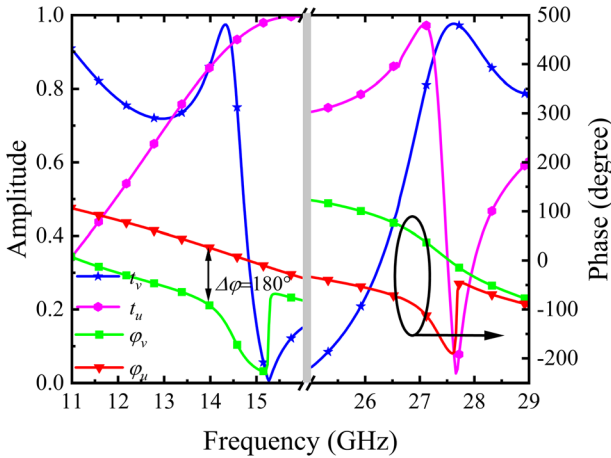


FIGURE 3 Full-wave simulating results of the transmitting coefficient and phase difference, when the incident wave polarization direction is along  $u$ - axes and  $v$ - axes, respectively

incident wave has the same response as the  $y$ -polarized incident wave.

Figure 4 plots the full-wave simulating cross-polarization transmitting coefficients and phase difference of the two states of the proposed unit cell when the polarization direction of the incident wave along the  $y$ -axes. It shows that in the bands of 13.6–14.8 GHz and

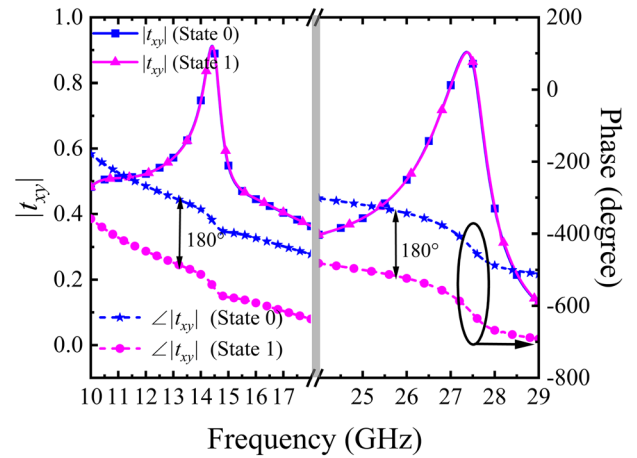


FIGURE 4 Full-wave simulating results of the cross-polarization transmitting coefficient and phase difference for the two metasurface states

26.7–27.7 GHz, two states with high cross-polarization transmitting efficiency (larger than 0.7) and out-of-phase response are obtained. Since the structure is symmetric along both the  $x$ - and  $y$ - axes, the cross-polarization transmitting coefficient for the  $x$ -polarized incident wave has the same response as the  $y$ -polarized incident wave.

Figure 5A plots the influence on the transmitting coefficient introduced by changing  $l$ , showing that the length of  $l$  determines the lower transmitting frequency. Similarly, in the upper frequency band, as shown in Figure 5B also plots the influence on the transmitting coefficient by changing  $w$ , showing that the length of  $w$  determines the upper transmitting frequency. Since the structure is symmetric along both the  $x$ - and  $y$ - axes, the cross-polarization transmitting coefficient for the  $x$ -polarized incident wave has the same response as the  $y$ -polarized incident wave.

## 2.2 | Equivalent circuit model analysis

Figure 6 illustrates the corresponding equivalent circuit model (ECM) model of the proposed metasurface, where

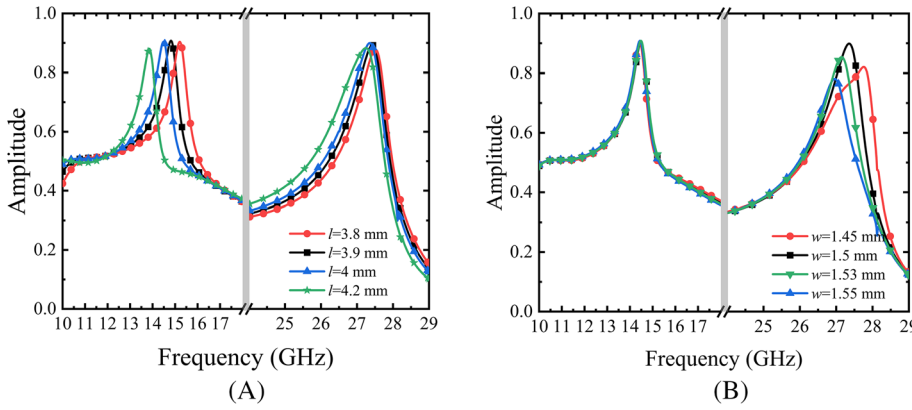


FIGURE 5 Parameter sweeping effects for both lower and upper bands. (A) Lower band. (B) Upper band

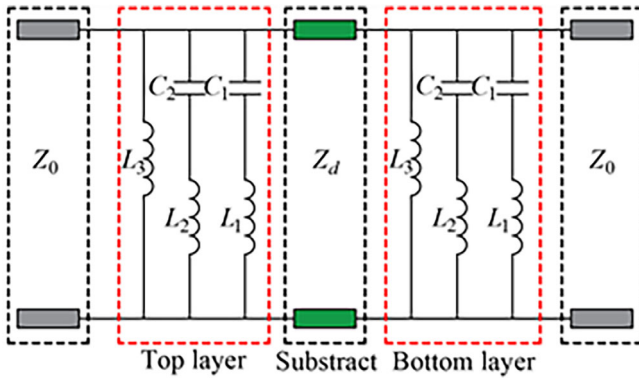


FIGURE 6 Equivalent circuit of the proposed metasurface unit cell

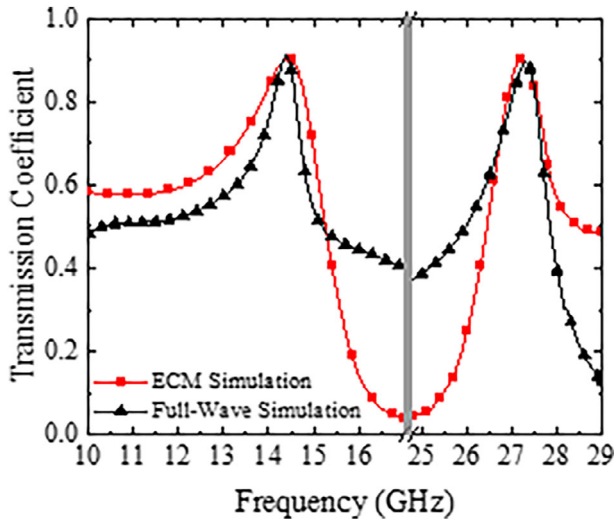


FIGURE 7 Comparison of the unit cell transmission coefficient between the equivalent circuit model simulation and full-wave simulation results

$Z_0$  is the wave impedance of free space, which is  $377\Omega$ ,  $Z_d$  is the impedance of equivalent transmission line corresponding to the substrate, which is  $Z_0/\sqrt{\epsilon_r}$ . The outer square rings and middle square rings of the metasurface

are modeled by a pair of resonators composed of  $L_2$ ,  $C_2$ , and  $L_3$ , whose values are  $L_2 = 2$  nH,  $C_2 = 0.037$  pF,  $L_3 = 118$  nH, respectively and obtained by<sup>40</sup>:

$$C_2 = \frac{1.6p}{\omega\lambda} \left[ \ln \csc \left( \frac{\pi g}{2p} \right) + \frac{1}{\sqrt{1 - \left( \frac{p}{\lambda} \right)^2}} \right] \quad (3)$$

$$L_2 = \frac{X_1}{\omega} = \frac{p}{\omega\lambda} \left[ \ln \csc \left( \frac{\pi s}{p} \right) + \frac{1}{\sqrt{1 - \left( \frac{p}{\lambda} \right)^2}} \right] \quad (4)$$

$$L_3 = \frac{2(X_1 || X_2)}{\omega} \quad (5)$$

where  $X_2$  is derived as

$$X_2 = 0.8 \frac{p}{\lambda} \left[ \ln \csc \left( \frac{\pi s}{p} \right) + \frac{1}{\sqrt{1 - \left( \frac{p}{\lambda} \right)^2}} \right] \quad (6)$$

in which  $\lambda$  is the wavelength of the wave in the free space. The rhombus patches are modeled as the other pair of resonators with the inductor  $L_1$  and capacitor  $C_1$ , which are optimized as  $L_1 = 10.51$  nH, and  $C_1 = 0.002$  pF. Figure 7 plots the comparison of the unit cell transmission coefficient between the ECM simulation and full-wave simulation results. It shows that the ECM simulation result agrees well with the full-wave simulation, which demonstrates the effectiveness of the ECM.

### 3 | METASURFACE DESIGN

A full metasurface with  $30 \times 30$  elements to generate the +1 mode OAM beam is designed based on the proposed

FIGURE 8 Full metasurface design. (A) States distribution. (B) Photo of fabricated metasurface prototype

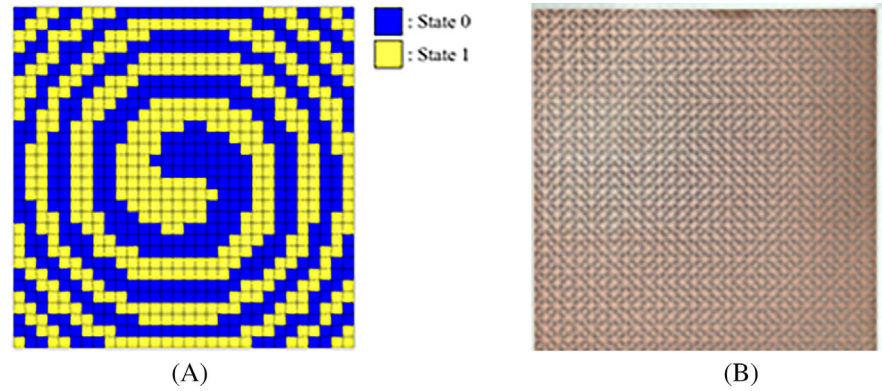
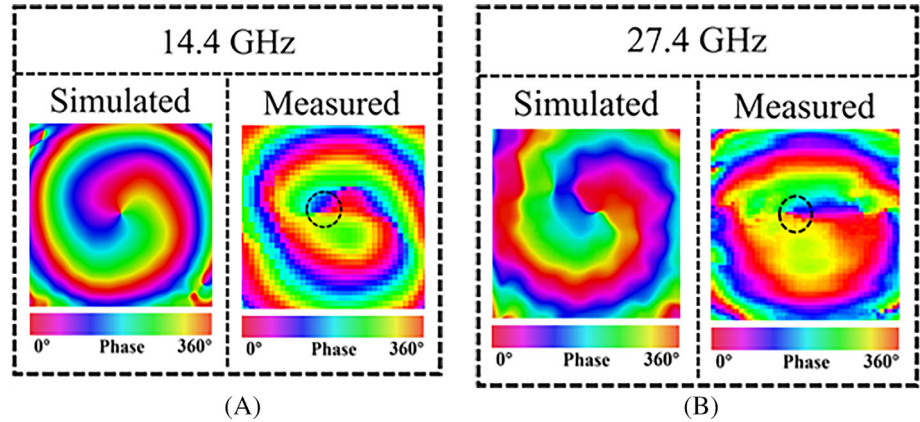


FIGURE 9 The simulated and measured near-field phase distribution of the metasurface at the two operating frequencies. (A) 14.4 GHz. (B) 27.4 GHz



unit cell. The design process may be divided into the following three steps. The first step is to calculate the ideal OAM phase distribution  $\varphi_i(x, y)$  for a planar incident wave, which may be calculated by

$$\varphi_i(x, y) = l \cdot \tan\left(\frac{y}{x}\right) \quad (7)$$

where  $l$  is the mode of the OAM. The second step is to compensate for the phase deviation introduced by the spherical wavefront radiated by the feeding antenna. The compensating phase distribution  $\varphi_c(x, y)$  is obtained by

$$\varphi_c(x, y) = \frac{2\pi}{\lambda} \cdot \left( \sqrt{(x^2 + y^2) + F^2} - F \right) \quad (8)$$

where  $F$  is the distance between the metasurface and feeding antenna as shown in Figure 1. The practical OAM phase distribution of the metasurface is then calculated by summing the ideal phases and the compensating phases, which is

$$\varphi_p(x, y) = \varphi_i(x, y) + \varphi_c(x, y) \quad (9)$$

Finally, the 1-bit quantization is realized by equally dividing a phase period ( $0^\circ$ – $360^\circ$ ) into two subdivisions,

and the practical phase  $\varphi_p(x, y)$  within each subdivision is assigned to be a discrete phase, either  $0^\circ$  or  $180^\circ$ . The quantized phase  $\varphi_q(x, y)$  is then computed as

$$\varphi_q(x, y) = \begin{cases} 0^\circ, & 0^\circ \leq \varphi_p(x, y) < 180^\circ \\ 180^\circ, & 180^\circ \leq \varphi_p(x, y) \leq 360^\circ \end{cases} \quad (10)$$

Figure 8 shows the structure of the designed metasurface based on the phase distribution obtained by Equation 10. Figure 8A shows the state distribution of the metasurface, where state 0 is corresponding to the phase  $\varphi_q(x, y) = 0^\circ$ , while state 1 is corresponding to the phase  $\varphi_q(x, y) = 180^\circ$ . Figure 8B shows the photo of the fabricated metasurface prototype.

## 4 | METASURFACE RESULTS AND DISCUSSION

In order to validate the propose CM, full-wave simulation using software CST Microwave Studio is performed for the designed metasurface, and the near-field phase distribution and far-field patterns of the fabricated metasurface are measured in the experiment. The LP horn antenna (LB-62-20-C-SF) working at the lower frequency and the LP horn antenna (LB-180400H-KF) working at

the upper frequency are set as the feeding source. Figure 9 plots the simulated and measured near-field distribution of the metasurface at the two operating frequencies, 14.4 and 27.4 GHz, respectively. In the near-field measurement, the distance between the feeding antenna and the metasurface  $F$  is set as 200 mm. In both frequencies, the  $l = +1$  mode spiral phase distribution are clearly observed. These generated phase distributions of E-field exhibit the characteristics of OAM beams with spiral phase distributions, which is due to the phase singularity at the central region. There is some distortion in the measured results, which may be caused by the fact that the feeding position is not completely consistent with the center of the metasurface.

Figure 10 shows the far-field experiment setup. A pair of LP horn antennas are set as the transmitter and receiver, respectively. Both the receiver and transmitter are connected to the two ports of a vector network

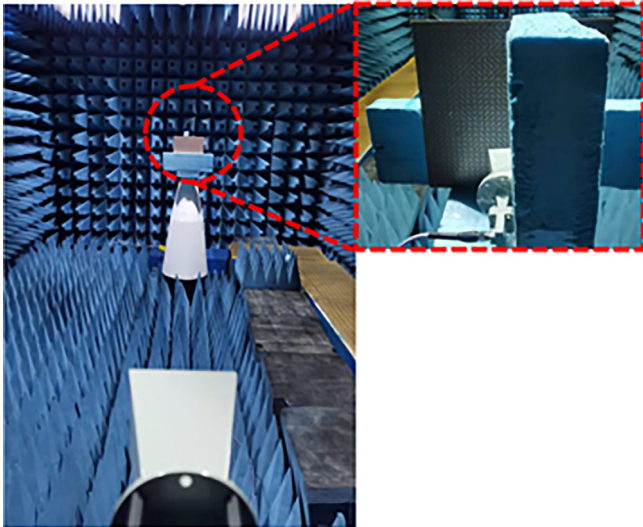


FIGURE 10 The measurement setup for the orbital angular momentum metasurface

analyzer (VNA). The transmitter and the metasurface prototype are fixed together on a turntable. By rotating the turntable, the far-field radiating pattern of the metasurface is picked up by the receiver and measured by the VNA.

Figure 11 plots the simulated and measured far-field pattern of the metasurface at the two operating frequencies, 14.4, and 27.4 GHz, respectively, where Figure 11A plots the far-field pattern at 14.4 GHz and Figure 11B plots the far-field pattern at 27.4 GHz. The simulated and measured results agree well with each other and a null is observed at the normal direction for both frequencies as expected. The measured maximum transmitting gain of the metasurface is around 20 and 16 dBi at 14.4 and 27.4 GHz, respectively.

To further verify the reliability of the proposed method, the power spectrum of these OAM beams generated by the designed metasurface is calculated using the discrete Fourier transform algorithm. The Fourier relationship between the OAM spectrum  $A_l$  and the corresponding sampling phase  $\psi(\varphi)$  can be expressed as<sup>17</sup>:

$$\psi(\varphi) = \sum_{-\infty}^{+\infty} A_l \exp(jl\varphi) \quad (11)$$

$$A_l = \frac{1}{2\pi} \int_0^{2\pi} \psi(\varphi) \exp(-jl\varphi) d\varphi \quad (12)$$

where  $\psi(\varphi)$  refers to the discrete sampling phase value in the sampling plane,  $\exp(-jl\varphi)$  is the harmonic related to the spiral phase front.

According to the sampling phase, the mode purity of OAM is calculated by normalizing each OAM mode spectrum to the total spectrum of all OAM modes, namely

$$\text{Mode purity (Energy Weight)} = \frac{A_l}{\sum_{l=-3}^3 A_l} \quad (13)$$

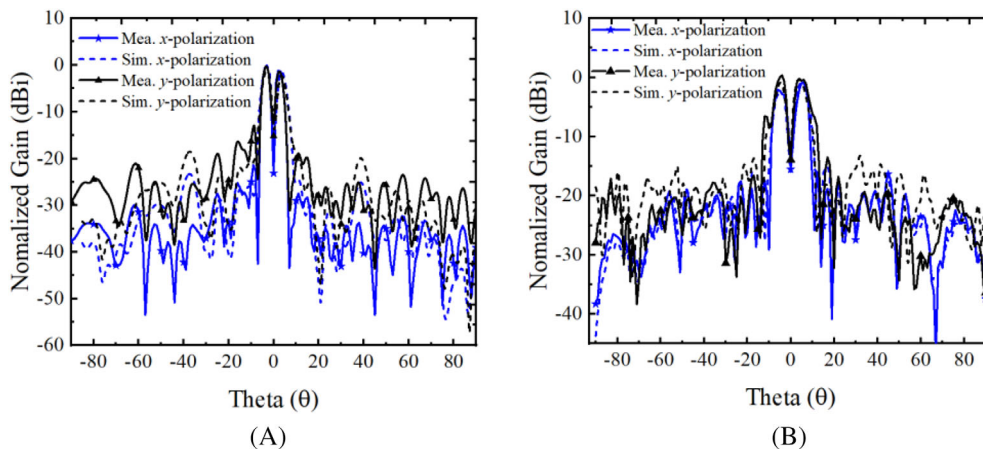


FIGURE 11 The simulated and measured far-field pattern of the metasurface at the two operating frequencies. (A) 14.4 GHz. (B) 27.4 GHz

FIGURE 12 Simulated mode purity of orbital angular momentum beams for the proposed metasurface at (A) 14.4 GHz, (B) 27.4 GHz

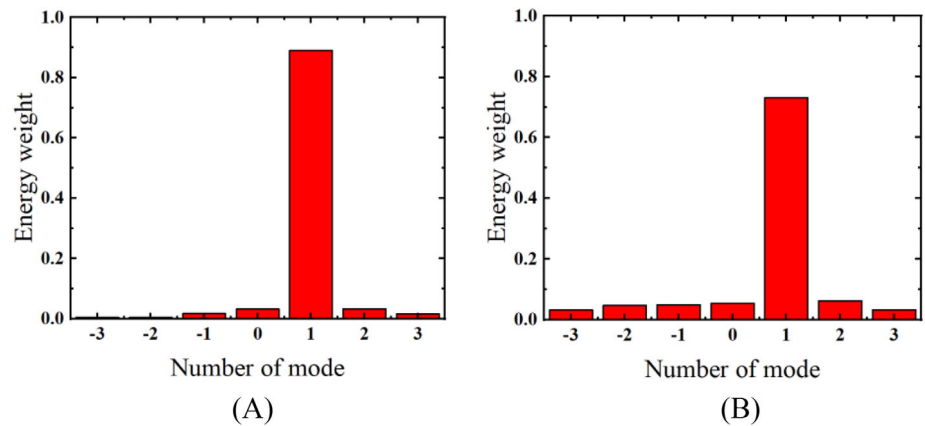


TABLE 1 Comparison for transmitting metasurfaces realized in the literature

References	Bandwidth (GHz, 3-dB)	Thickness (mm)	OAM (mode)	Purity	Gain (dBi)
19	Narrow	4.5	1	NA	14.5
20	Narrow	2	1, 2, 4	NA	18.45
21	5.2–5.8	1.5	$\pm 1, \pm 2$	>0.6	7–8
22	4.9–5.4	3.73	1, 2	NA	NA
23	7–11.5	30	2	>0.75	NA
This work	13.6–14.8, 26.7–27.7	1.524	1	>0.73	16–20

Abbreviation: OAM, orbital angular momentum.

Figure 12 plots the simulated mode purity of OAM beams for the proposed metasurface, where Figure 12A plots the mode purity at 14.4 GHz, while Figure 12B plots the mode purity at 27.4 GHz. It can be seen that most of the power is concentrated within the generated OAM mode, only a few parts of the power extend to the neighboring OAM channels. The calculated mode purities of OAM beams with  $l = +1$  are 0.89 at the lower frequency and 0.73 at the upper frequency, respectively.

Finally, a comparison between our work and recently reported ones in the thickness, frequency, mode purity, and gain are provided in Table 1. Our design has the clear advantages of the dual-band, compact design, and relatively high gain compared to other works.

## 5 | CONCLUSION

A double-layer 1-bit transmitting CM for the effective generation of dual-band OAM waves is presented in this article. The proposed metasurface unit cell is studied by both operating principle and ECM analysis and is demonstrated by both full-wave simulation and experiment. When the OAM mode of  $l = +1$  with mode purities over 0.73 at the dual-band. The proposed double-layer metasurface with the advantages of simple structure and high

efficiency may find wide potential in future millimeter-wave wireless transmission systems.

## ACKNOWLEDGMENT

This work was supported by the National Natural Science Foundation of China under grant no. 61771226.

## DATA AVAILABILITY STATEMENT

Research data are not shared.

## ORCID

Xiaopeng Shen  <https://orcid.org/0000-0003-1836-1878>

## REFERENCES

- Allen L, Beijersbergen MW, Spreeuw RJC, Woerdman JP. Orbital angular momentum of light and the transformation of Laguerre-Gaussian laser modes. *Phys Rev A*. 1992;45(11):8185-8189.
- Yao AM, Padgett MJ. Orbital angular momentum: origins, behavior and applications. *Adv Opt Photon*. 2011;3:161-204.
- Jack B, Leach J, Romero J, et al. Holographic ghost imaging and the violation of a bell inequality. *Phys Rev Lett*. 2009;103(8):803602.
- Nagali E, Sansoni L, Sciarrino F, et al. Quantum information transfer from spin to orbital angular momentum of photons. *Phys Rev Lett*. 2009;103(1):013601.
- Willner AE, Huang H, Yan Y, et al. Optical communications using orbital angular momentum beams. *Adv Opt Photonics*. 2015;7(1):66-106.

6. Opare KA, Kuang Y, Kponyo JJ. Mode combination in an ideal wireless OAM-MIMO multiplexing system. *IEEE Wireless Commun Lett.* 2015;4(4):449-452.
7. Edfors O, Johansson AJ. Is orbital angular momentum (OAM) based radio communication an unexploited area? *IEEE Trans Antennas Propag.* 2011;60(2):1126-1131.
8. Barbuto M, Miri MA, Alu A, Bilotti F, Toscano A. Exploiting the topological robustness of composite vortices in radiation systems. *Prog Electromagn Res.* 2018;162:39-50.
9. Morabito AF, Di Donato L, Isernia T. Orbital angular momentum antennas: understanding actual possibilities through the aperture antennas theory. *IEEE Antennas Propag Mag.* 2018;60(2):59-67.
10. Hui X, Zheng S, Hu Y, et al. Ultralow reflectivity spiral phase plate for generation of millimeter-wave OAM beam. *IEEE Antennas Wirel Propag Lett.* 2015;14:966-969.
11. Bai Q, Tennant A, Allen B. Experimental circular phased array for generating OAM radio beams. *Electron Lett.* 2014;50(20):1414-1415.
12. Bai XD, Liang XL, Li JP, et al. Rotman lens-based circular array for generating five-mode OAM radio beams. *Sci Rep.* 2016;6(1):1-8.
13. Yu S, Li L, Shi G, Zhu C, Shi Y. Generating multiple orbital angular momentum vortex beams using a metasurface in radio frequency domain. *Appl Phys Lett.* 2016;108(24):241901.
14. Chen MLN, Jiang LJ, Wei EI. Ultrathin complementary metasurface for orbital angular momentum generation at microwave frequencies. *IEEE Trans Antennas Propag.* 2016;65(1):396-400.
15. Li A, Forati E, Sievenpiper D. Study of the electric field enhancement in resonant metasurfaces. *J Opt.* 2017;19(12):125104.
16. Xu HX, Liu H, Ling X, Sun Y, Yuan F. Broadband vortex beam generation using multimode Pancharatnam–berry Metasurface. *IEEE Trans Antennas Propag.* 2017;65(12):7378-7382.
17. Yang LJ, Sun S, Wei EI. Ultrawideband reflection-type metasurface for generating integer and fractional orbital angular momentum. *IEEE Trans Antennas Propag.* 2020;68(3):2166-2175.
18. Ma H, Kong X, Chen P, et al. Broadband vortex beams generation with narrow divergence angle using polarization insensitive metasurface. *IEEE Access.* 2020;8:218062-218068.
19. Qin F, Wan L, Li L, Zhang H, Wei G, Gao S. A transmission metasurface for generating OAM beams. *IEEE Antennas Wirel Propag Lett.* 2018;17(10):1793-1796.
20. Lv HH, Huang QL, Yi XJ, Hou JQ, Shi XW. Low-profile transmitting metasurface using single dielectric substrate for OAM generation. *IEEE Antennas Wirel Propag Lett.* 2020;9(5):881-885.
21. Guo K, Zheng Q, Yin Z, Guo Z. Generation of mode-reconfigurable and frequency-adjustable OAM beams using dynamic reflective metasurface. *IEEE Access.* 2020;8:75523-75529.
22. Shi H, Wang L, Zhao M, Chen J, Zhang A, Xu Z. Transparent metasurface for generating microwave vortex beams with cross-polarization conversion. *Mater.* 2018;11(12):2448.
23. Jiang S, Chen C, Zhang H, Chen W. Achromatic electromagnetic metasurface for generating a vortex wave with orbital angular momentum (OAM). *Opt Express.* 2018;26(5):6466-6477.
24. Ji C, Song J, Huang C, Wu X, Luo X. Dual-band vortex beam generation with different OAM modes using single-layer metasurface. *Opt Express.* 2019;27(1):34-44.
25. Xin M, Xie R, Zhai G, et al. Full control of dual-band vortex beams using a high-efficiency single-layer bi-spectral 2-bit coding metasurface. *Opt Express.* 2020;28(12):17374-17383.
26. Choudhary DK, Chaudhary RK. A compact CPW-based dual-band filter using modified complementary split ring resonator. *Int J Electron Commun.* 2018;89:110-115.
27. Choudhary DK, Chaudhary RK. Miniaturized quad-band filter with improved selectivity using split ring resonators and metallic strips. *Int J RF Microw Comput-Aid Eng.* 2021;31(10):e22809.
28. Choudhary DK, Chaudhary RK. A compact triple band metamaterial inspired bandpass filter using inverted S-shape resonator. *Radioengineering.* 2018;27(2):373-378.
29. Pfeiffer C, Grbic A. Controlling vector Bessel beams with metasurfaces. *Phys Rev A.* 2014;2(4):044012.
30. Gao LH, Cheng Q, Yang J, et al. Broadband diffusion of terahertz waves by multi-bit coding metasurfaces. *Light Sci Appl.* 2015;4(9):e324.
31. Liu S, Zhang L, Yang QL, et al. Frequency-dependent dual-functional coding metasurfaces at terahertz frequencies. *Adv Opt Mater.* 2016;4(12):1965-1973.
32. Wang X, Caloz C. Spread-spectrum selective camouflaging based on time-modulated metasurface. *IEEE Trans Antennas Propag.* 2021;69(1):286-295.
33. Wang X, Yang GM. Time-coding spread-spectrum reconfigurable intelligent surface for secure wireless communication: theory and experiment. *Opt Express.* 2021;29(20):32031-32041.
34. Wang X, Caloz C. Pseudorandom sequence (space-) time-modulated metasurfaces: principles, operations, and applications. *IEEE Antennas Propag Mag.* 2022;64(4):135-144.
35. Zhang D, Cao X, Yang H, Gao J, Zhu X. Multiple OAM vortex beams generation using 1-bit metasurface. *Opt Express.* 2018;26(19):24804-24815.
36. Bai X, Kong F, Sun Y, et al. High-efficiency transmissive programmable metasurface for multimode OAM generation. *Adv Opt Mater.* 2020;8(17):2000570.
37. Bi F. Ka-band 1-bit ultra-thin reflective metasurface for generating vortex beams based on wideband polarization converter. *Int J RF Microw Comput-Aid Eng.* 2022;32(7):e23185.
38. Wu LW, Ma HF, Gou Y, et al. High-transmission ultrathin Huygens' metasurface with 360 phase control by using double-layer transmitarray elements. *Phys Rev A.* 2019;12(2):024012.
39. Gao X, Han X, Cao WP, Li HO, Ma HF, Cui TJ. Ultrawideband and high-efficiency linear polarization converter based on double V-shaped metasurface. *IEEE Trans. Antennas Propag.* 2015;63(8):3522-3530.
40. Yilmaz AE, Kuzuoglu M. Design of the square loop frequency selective surfaces with particle swarm optimization via the equivalent circuit model. *Radioengineering.* 2009;18(2):95-102.

**How to cite this article:** Li J, Kong X, Wang J, et al. Dual-band polarization-insensitive orbital angular momentum beam generation based on 1-bit polarization-converting transmitting coding metasurface. *Int J RF Microw Comput Aided Eng.* 2022;e23397. doi:[10.1002/mmce.23397](https://doi.org/10.1002/mmce.23397)